batteries

MDPI

Article

Symmetric and Asymmetric Supercapacitors of ITO Glass and Film Electrodes Consisting of Carbon Dot and Magnetite

Misganu Chewaka Fite [1], Po-Jen Wang [2] and Toyoko Imae [1,2,*]

[1] Graduate Institute of Applied Science and Technology, National Taiwan University of Science and Technology, Taipei 10607, Taiwan
[2] Department of Chemical Engineering, National Taiwan University of Science and Technology, Taipei 10607, Taiwan
* Correspondence: imae@mail.ntust.edu.tw

Abstract: To enhance the energy density, hybrid supercapacitors were fabricated, and their electrochemical features were investigated using a two-electrode configuration. By assembling nitrogen-doped graphene/magnetite (NG/Fe_3O_4) on indium tin oxide-coated (ITO) glass as a cathode and NG/carbon dots(Cdots)/Fe_3O_4 on ITO glass as an anode, a much higher gravimetric specific capacitance of 252.2 F/g, at a current density of 0.5 A/g, was obtained from this asymmetric supercapacitor compared with that (212.0 F/g) of a symmetric supercapacitor (NG/Cdots/Fe_3O_4)//(NG/Cdots/Fe_3O_4). A gravimetric energy density of 90.1 Wh/kg was obtained for an asymmetric ITO glass device at a specific power density of 400.0 W/kg. On the other hand, when an asymmetric two-electrode cell was fabricated with a Cdots/polypyrrole (PPy)/Fe_3O_4/TEMPO-oxidized cellulose nanofiber (TOCNF)-film electrode and a Cdots/PPy/TOCNF-film electrode, the specific capacitance (107.1 F/g) at a current density of 0.8 A/g was lower than that (456.4 F/g) of a symmetric (Cdots/PPy/Fe_3O_4/TOCNF)//(Cdots/PPy/Fe_3O_4/TOCNF)-film cell. Subsequently, a gravimetric energy density of 40.6 Wh/kg was achieved for a symmetric-film device at a specific power density of 320 W/kg. These results suggest that our method offers an efficient approach to developing symmetric and asymmetric devices consisting of hybrid materials for meeting the ever-increasing demands on energy-storage devices.

Keywords: two-electrode system; symmetric supercapacitor; asymmetric supercapacitor; carbon dot; magnetite

Citation: Fite, M.C.; Wang, P.-J.; Imae, T. Symmetric and Asymmetric Supercapacitors of ITO Glass and Film Electrodes Consisting of Carbon Dot and Magnetite. *Batteries* **2023**, *9*, 162. https://doi.org/10.3390/batteries9030162

Academic Editors: Catia Arbizzani and Liubing Dong

Received: 6 February 2023
Revised: 27 February 2023
Accepted: 5 March 2023
Published: 8 March 2023

1. Introduction

The rapid increase in the population and advancements in technology suggest the necessity of clean and high-efficiency energy-conversion and storage devices [1]. Supercapacitors are strong candidates for storing electrical energy and reducing the exhaustion of fossil fuels. Hybrid supercapacitors with high storage and release rates [2], augmented capacitive properties, low preservation costs, and enhanced energy density and power density [1] attract significant attention from scholars and industrialists. However, the energy density of supercapacitors is comparatively far lower than that of batteries. Thus, for practical use, it is necessary to design innovative materials and novel technologies to enhance the energy density for applications with high power supply and cycling life. In particular, the specific capacitance and the potential window can strongly influence the power density and energy-storage ability of supercapacitor devices [2,3].

The integration of electrical double-layer capacitor (EDLC) materials (carbonaceous materials) with a large surface area and good electronic conductivity [2] with psuedocapacitance (PC) materials (conducting polymers and metal oxides/hydroxides/sulfides) [4] with high specific capacitance to develop hybrid supercapacitors has shown enhanced specific capacitance due to the complementary effect [5,6]. Based on the storage mechanism, owing to the surface-reaction process (redox reaction), PC materials have revealed higher energy

density than EDLC materials. Since it reduces production costs, the usage of environmentally friendly and abundant materials [4] is strongly suggested in electrode-materials engineering. Nitrogen-doped graphene (NG), which is an EDLC material containing free valence electron, can interact with electrolytes easily [5]. Carbon dots (Cdots) are carbon-based materials containing different functional groups and have gained attention because of their outstanding electro-optical properties [7], rapid transfer of electrons [8], small size [9], lower price, simple preparation [10], and favorability for potential applications [9–11]. Magnetite (Fe_3O_4) and polypyrrole (PPy) are promising candidate PC materials due to their low cost, good conductance, abundance, eco-friendly properties, high capacitance in aqueous electrolyte solutions and wide operation-potential window [12]. Both materials can facilitate charge and ion transport in full electrodes.

The synergistic effects of individual components in composites offer high performance levels in supercapacitors. For instance, the specific capacitance of a flower-like Fe_3O_4/reduced graphene oxide (rGO) hybrid nanocomposite electrode was 425 F/g at a current density of 1.5 A/g [13], an Fe_2O_3/rGO/Fe_3O_4@Fe electrode showed an electrochemical performance of 337.5 mF/cm^2 at 20 mA/cm^2 [14], an in situ-grown nitrogen-doped GO@Fe_3O_4-carbon-nanotube electrode exhibited a specific capacitance of 418 F/g [15], and a composite electrode of GO/PPy for a supercapacitor exhibited a specific capacitance of 332.6 F/g [16]. These electrodes provide better electrochemical performances than their individual components. In particular, it should be noted that the synergetic effect of Cdots on capacitance is remarkable. The composites of polyaniline, polyaniline@carbon nanohorn and PPy@carbon nanohorn with Cdots resulted in higher capacitance than the additive capacitance values of each component, despite the low conductivity of Cdots, because of their electron-carrying ability [6,17].

Widening the potential window makes a strong contribution to increasing energy density. The best way to a operate wide potential window is to assemble a hybrid supercapacitor to benefit from the complementary effect of the potential window. That is, a capacitor-type negative electrode (anode) separated by a porous separator from a battery-type positive electrode (cathode) should be prepared because they can operate different potential windows in the same electrolyte [18]. Recently, some studies reported symmetric and asymmetric hybrid supercapacitors [3,19–22]. For instance, carbonaceous materials, such as commercial activated carbon, carbon nanotubes, graphene and NG sheets were frequently used as negative electrodes in asymmetric hybrid supercapacitors [20]. In addition, different metal oxides/hydroxides/sulfides (Fe_2O_3, Fe_3O_4, MnO_2, V_2O_5, $Ni(OH)_2$ and VS_2), conducting polymers (polypyrrole (PPy) and polyaniline) and hybrid composites were used as positive electrodes. However, the energy density and power density obtained were still lower; therefore, the development of suitable electrode materials and novel techniques is required.

In our previous work [5,23], electrochemical measurements of a NG/Fe_3O_4 (EDLC/PC) hybrid electrode over a positive potential window (0 to 0.8 V) and a NG/Cdots/Fe_3O_4 hybrid electrode over a window with greater negative potential (−0.5 to 0.3 V) have showed good capacitance performance with a three-electrode configuration. In particular, the NG/Cdots/Fe_3O_4 hybrid enhanced the specific capacitance and stabilized the supercapacitor electrode [5,6,23]. Thus, in this work, electrodes of NG/Fe_3O_4 [5], NG/Cdots and NG/Cdots/Fe_3O_4 [23] hybrids were assembled on indium tin oxide-coated (ITO) glass in a two-electrode configuration to compare the electrochemical performance of an asymmetric hybrid supercapacitor with that of a symmetric hybrid supercapacitor. For comparison, a Cdots/Fe_3O_4/PPy hybrid, which is richer in supercapacitance than the NG/Cdots/Fe_3O_4 hybrid, was employed as an electrode material. Moreover, the Cdots/Fe_3O_4/PPy hybrid was fabricated on a TEMPO-oxidized cellulose nanofiber (TOCNF) film. It is suggested that the hybrid electrodes assembled in the two-electrode systems selected in this work increase energy density for practical applications.

2. Experimental Section

2.1. Materials

Dried pulp was obtained from Canary Corporation, Taiwan. An aqueous sodium hypochlorite solution (NaOCl, 12 wt%) was obtained from Shimakyu Pure Chemicals, Japan and 2,2,6,6-tetramethyl-1-piperidine-1-oxyl radical (TEMPO) was purchased from Alfa Aesar, USA. Sodium borohydride ($NaBH_4$), sodium bromide (NaBr), pyrrole (99%), citric acid (99.5%), ethylenediamine (99%), iron(II) sulfate heptahydrate (99%) and ammonium persulfate (APS, 98%) were obtained from Acros Organics, Doral, NW, USA. Sodium hydroxide (NaOH) was purchased from Fisher Chemical, Waltham, MA, USA. Ultrapure water was from a Millipore purification system (Yamato Millipore WT100, Tokyo, Japan). The ITO glass was purchased from AimCore Technology, Taiwan.

The NG/Fe_3O_4, NG/Cdots and NG/Cdots/Fe_3O_4 hybrid electrodes were previously prepared and characterized by means of IR absorption spectrum, thermogravimetric analysis, transition electron microscopy, nitrogen adsorption–desorption isotherm, X-ray photoelectron spectrum, X-ray diffraction, magnetization–magnetic-field curve and fluorescence microscopy measurements [5,18]. The NG/Fe_3O_4 was synthesized by in situ deposition of 42 wt% Fe_3O_4 on 58 wt% NG. The NG/Cdots was a mixture of 96 wt% NG and 4 wt% Cdots, which was synthesized from equimolar mixture of ethylene diamine and citric acid. The NG/Cdots/Fe_3O_4 was a mixture of 58 wt% NG/Cdots and 42 wt% Fe_3O_4.

2.2. Synthesis of Cdots/PPy/TOCNF and Cdots/PPy/Fe_3O_4/TOCNF Composite Films

The TOCNF was prepared by the TEMPO-mediated oxidation method [24,25]. For an aqueous dispersion of dry pulp (10 g), NaBr (1 g) and TEMPO (320 mg, 100 mL), NaClO (13 wt%, 52 mL) was slowly dropped and the mixture was stirred for 2 days, with pH kept at 10 during the reaction. The crude product was collected by centrifugation (6000 rpm, 10 min) and washed with water. For the reduction of the side product (aldehyde unit), the crude product was dispersed in water (750 mL) with $NaBH_4$ (2 g) and stirred for 8 h. Next, the dispersion was collected by centrifugation (6000 rpm, 10 min), washed with water, dispersed in water and, finally, sonicated for 30 min on an ultrasonic processor (QSONICA Q700, Melville, NY, USA) in an ice bath at 40 amplitudes to obtain a stable TOCNF gel.

The Fe_3O_4 nanowires (NWs) were synthesized with the hydrothermal method [26]. The $FeSO_4 \cdot 7H_2O$ (4 mmol) and $Na_2S_2O_3 \cdot 5H_2O$ (2 mmol) were mixed with an aqueous dispersion of PEG400 (PEG400:water = 1:3 volume ratio) under stirring and NaOH (50 mmol) was added. The mixture was reacted in an autoclave at 150 °C for 1 day. The final product was collected with a magnet, washed with water and ethanol and then air-dried overnight. The Fe_3O_4 NWs were homogeneously dispersed in a TOCNF gel (dried TOCNF:Fe_3O_4 = 10:1 mass ratio) under stirring for 1 day and dried in a Petri dish at room temperature. Similarly, the TOCNF film without Fe_3O_4 was also prepared in a Petri dish. These films were used as substrates for subsequent preparation.

The Cdots were prepared by hydrothermal method [27]. A mixture of citric acid (1 g) and ethylenediamine (600 μL) dissolved in water (50 mL) was incubated in an autoclave under 230 °C for 5 h. The Cdots (100 μL) and pyrrole monomer (280 μL) were sequentially dropped on the surface of TOCNF film in the Petri dish and maintained at 0–5 °C. Subsequently, the Petri dish was filled with an APS solution of 1 M HCl (2 wt%, 8.0 mL) and kept for 4 h. Next, the film was washed thoroughly with water and dried overnight. The product was named Cdots/PPy/TOCNF. The Cdots/PPy was also synthesized on Fe_3O_4/TOCNF film instead of TOCNF film, and the product was called Cdots/PPy/Fe_3O_4/TOCNF.

2.3. Instruments

Materials were characterized using field-emission scanning electron microscopy (FE-SEM, JSM-7900F, Jeol, Japan), Fourier-transform infrared absorption spectrometry (FTIR, Thermo Fisher Scientific, Nicolet-6700, Waltham, MA, USA) with a range of 500 to 4000 cm^{-1} for 200 cycles and X-ray diffractometry (XRD, Bruker, D2 PHASER, Taylor, MI, USA) with CuKα (λ = 1.54184 Å) at 40 kV and 30 mA. The mechanical behavior was examined with a

tensile test meter (Testometric, M500-25AT, Rochdale, England) with a 10 N load cell at a rate of 5 mm/min upward and the films tested were rectangles measuring 1 cm × 4 cm. Young's modulus was calculated as a proportionality constant at the initial linear part on the stress–strain curve.

2.4. Electrochemical Measurements

Symmetric and asymmetric supercapacitor devices were assembled into two-electrode configuration. Homogenized slurry (0.02 mL) prepared from mixing composites (90 wt%) with polyvinylidene fluoride in N-methyl pyrrolidone (10 wt%) was cast on 1 cm × 1 cm of a cleaned ITO glass and was used for ITO glass electrodes. Two electrodes with equal masses of composites were separated by a separator of cellulose-acetate filter paper with 200-nanometer pores (Toyo Roshi Co., Ltd., Otowa, Japan); an electrolyte was dropped between the sandwiched electrodes, shielded by parafilm paper and aged overnight. Film-electrode cells were also prepared.

An instrument from Germany (ZAHNER messsysteme, model XPot workstation with a ThalesXT5.6.2 USB software) was used to perform electrochemical measurements. The electrochemical features, including potentiostat cycling voltammetry (CV), galvanostatic charge/discharge (GCD), electrochemical impedance spectroscopy (EIS) and capacitance cycling ability were evaluated in a NaCl electrolyte solution (1 M) at room temperature (~25 °C). The CV profile was swept from 5 to 100 mV/s over a maximum potential window of 1.6 V. The GCD profile was recorded at current densities ranging from 0.5 to 5 A/g and at a similar potential window to CV. The EIS was measured in a frequency ranging from 0.1 Hz to 100,000 Hz, with an alternating current with an amplitude of 0.01 V. The cycling stability was collected at a current density of 10 A/g. The voltametric specific capacitance (C_{vs}, F/g), gravimetric capacitance (C_{gs}, F/g), gravimetric energy density (U_g, Wh/kg) and power density (P_g, kW/kg) were calculated from Equation (1) [2,19,22].

$$C_{vs} = \int_{V_1}^{V_2} \frac{I(V)\,dV}{m\nu(V_2 - V_1)},\ C_{gs} = \frac{i{\cdot}\Delta t_{dt}}{V_2 - V_1},\ U_g = \frac{C_{gs}{\cdot}(V_2 - V_1)^2}{7.2},\ \text{and}\ P_g = \frac{U_g{\cdot}3.6}{\Delta t_{dt}} \quad (1)$$

where I(V), m, ν, V_1, V_2, Δt_{dt} and i are the current (A), the total mass of active material cast on a current collector (g), the scan rate (V/s), the starting potential window (V), the ending potential window (V), the change in the discharging time (s) and the current density (A/g), respectively.

The configuration of the two-electrode system is displayed in Figure 1. The leads of the working-electrode power (WE power) and the working-electrode sensing (WE sense) from the electrochemical workstation were connected to one side of the cell and the leads of reference electrode (RE) and counter electrode (CE) from the electrochemical workstation combined with another side of the cell. The two-electrode system comprised two same or different composite electrodes sandwiched fully in filter paper wetted with an electrolyte. The filter paper had two main purposes, namely, adsorption and storage of the electrolyte provided for the electrochemical reaction of the two-electrode system and separation of two composite electrodes simultaneously.

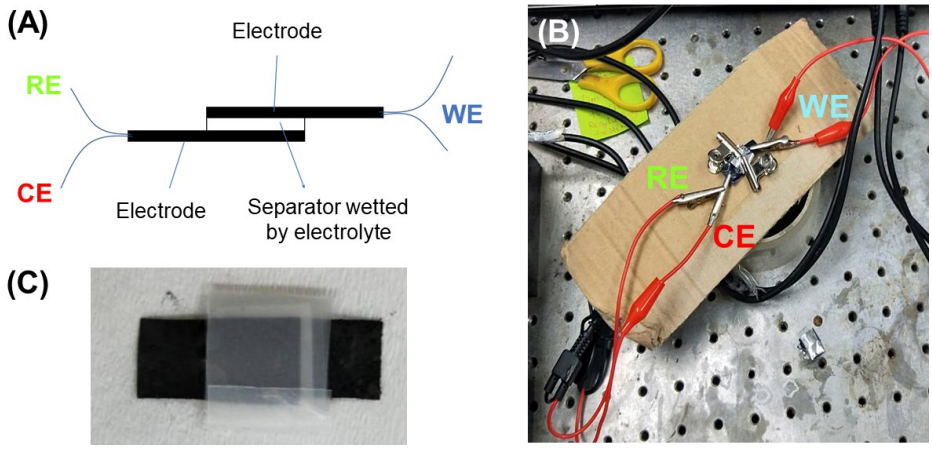

Figure 1. (**A**) A scheme and (**B**) an image of two-electrode configuration. (**C**) An image of a two-electrode cell.

3. Results and Discussion

3.1. Characterization of Film Electrodes

An XRD pattern of the Fe_3O_4 NWs is displayed in Figure 2A. The major characteristic peaks at 30.4°, 35.7°, 37.3°, 43.3°, 53.7°, 57.2° and 62.8° were assigned to (220), (311), (222), (400), (422), (511) and (440) indices of inverse spinel crystal structure of Fe_3O_4 (JCPDS No. 89-0691), respectively. Thus, the success of crystal Fe_3O_4 synthesis by the hydrothermal method was proven.

The TOCNF-films embedded Fe_3O_4 NWs and PPy were black owing to the black color of both additives. The magnetic properties of the Fe_3O_4 NWs and the Fe_3O_4/TOCNF film were confirmed by their attraction to the magnet, as shown in Figure 2B,C. Figure 2D(a) shows IR absorption spectra of Cdot and various TOCNF films. The characteristic IR bands of TOCNF were the OH bending-vibration mode at 1620 cm^{-1}, the CH bending-vibration mode at 1380 cm^{-1}, the C-O-H out-of-plane bending-vibration mode at 1120 cm^{-1} and the C-O-C stretching vibration mode at 1050 cm^{-1} [28]. The bands of the COO^- antisymmetric and symmetric stretching vibration modes were located at 1610 and 1420 cm^{-1}, respectively, and overlapped on the OH and CH bending-vibration bands, respectively, confirming the presence of the carboxylate group on the TOCNF. The three main bands of the Cdots at 1650, 1550 and 1400 cm^{-1}, respectively, were ascribed to C=O/C=N stretching-, N-H bending/C=C stretching- and C-N stretching-vibration modes [6]. These characteristic IR bands of the TOCNF and Cdots were observed in the IR spectra of the Cdots/TOCNF and the Cdots/Fe_3O_4/TOCNF. An additional characteristic band of the Cdots/Fe_3O_4/TOCNF at 553 cm^{-1} was attributed to an Fe-O stretching mode of the Fe_3O_4 NWs [29].

As shown in Figure 2D(b), an IR spectrum of the PPy/TOCNF displayed bands of PPy, as well as bands of TOCNF. The characteristic bands at 1550 and 1460 cm^{-1} were attributed to the C=C and C-N stretching-vibration modes of the PPy [17]. The bands at 1300, 1180, 1040 and 918 cm^{-1} were attributed to the deformation-vibration modes of the C-N in-plane, C-H in-plane, N-H in-plane and C-H out-of-plane of the PPy, respectively. Furthermore, the weaker bands at 787 and 673 cm^{-1} were attributed to the C-H out-of-plane deformation-vibration mode of the PPy ring. Thus, the PPy was successfully incorporated into the TOCNF film via the polymerization process. Due to partial overlap between the IR bands of the Cdots and the PPy, the IR spectrum of the Cdots/PPy/TOCNF was similar to that of the PPy/TOCNF. After the addition of the Fe_3O_4 NWs, the characteristic Fe-O stretching band of the Fe_3O_4 NWs was clearly observed in a spectrum of the Cdots/PPy/Fe_3O_4/TOCNF.

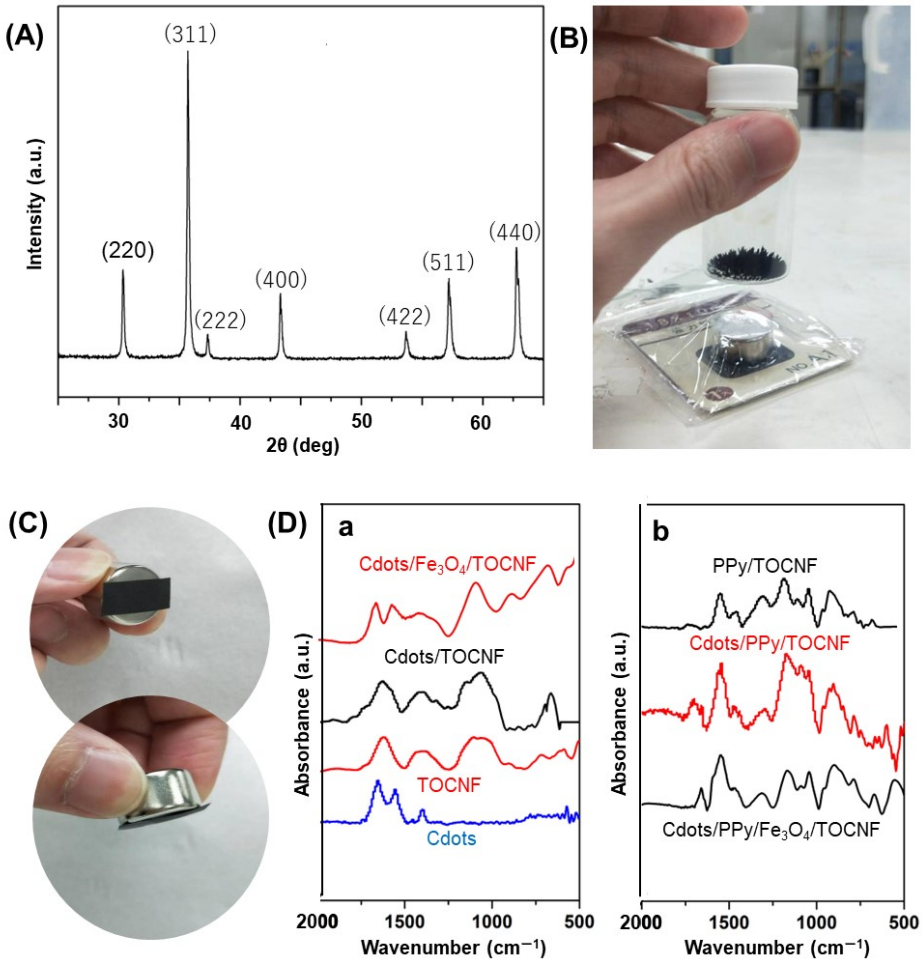

Figure 2. (**A**) An XRD pattern of Fe_3O_4 NWs, (**B**) an image of Fe_3O_4 NWs on a magnet, (**C**) images of an Fe_3O_4/TOCNF film on a magnet and (**D**) a,b IR absorption spectra of Cdots and various TOCNF films.

The mechanical properties of the composite films were evaluated (see Figure 3A). According to the stress–strain curve, the TOCNF film possessed a higher breaking strain (9.42%) and breaking stress (75.25 N/mm^2) than the Fe_3O_4/TOCNF and Cdots/PPy/Fe_3O_4/TOCNF films. The addition of the Fe_3O_4 decreased the breaking stress to 47.33 N/mm^2 and the breaking strain to 4.20%. When the Cdots/PPy layer was deposited on the Fe_3O_4/TOCNF film, the breaking stress and the breaking strain increased to 56.11 N/mm^2 and 6.60%, respectively. That is, the addition of PPy and Cdots on an Fe_3O_4/TOCNF film slightly recovers the mechanical performance of the composite film.

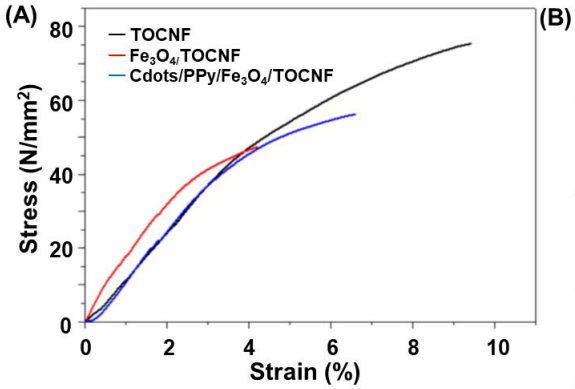

(B)

Film	Breaking stress (MPa)	Breaking strain (%)	Young's modulus (GPa)
TOCNF	75.25	9.42	12.30
Fe_3O_4/TOCNF	47.33	4.20	16.00
Cdots/PPy/Fe_3O_4/TOCNF	56.11	6.60	11.46

Figure 3. (**A**) Stress–strain curves and (**B**) a list of mechanical properties of TOCNF, Fe_3O_4/TOCNF and Cdots/PPy/Fe_3O_4/TOCNF films.

Young's modulus is a criterion for evaluating the elasticity of materials. A lower Young's modulus implies a more flexible material and, conversely, a higher Young's modulus indicates a material with better stiffness. While the TOCNF film had a Young's modulus of 12.30 GPa, the addition of Fe_3O_4 increased the Young's modulus of the TOCNF to 16.00 GPa. With the aid of the PPy and the Cdots, the minimum Young's modulus (11.46 GPa) of the composite film was attained, indicating that it had the highest flexibility of the three films. Especially in comparison with the brittle Fe_3O_4/TOCNF film, the polymerization of the pyrrole helped the mechanical modification to become more flexible, although the TOCNF film was able to withstand higher levels of stress at greater elongation than the Cdots/PPy/Fe_3O_4/TOCNF film.

The flexible Cdots/PPy/Fe_3O_4/TOCNF film did not vary visually, even though it was bent 50 times, as illustrated in Figure 4a. The FESEM images of the films before and after bending 50 times are compared in Figure 4b,c. Particles 50–100 nm in size completely cover the surface of the pristine composite film. This arrangement of the particles remained intact, as did the film before bending. These results suggest that the Cdots/PPy/Fe_3O_4/TOCNF composite film possesses sufficient structural strength to counter the effects of mechanical power.

3.2. Electrochemical Performance

Based on the NG/Fe_3O_4, NG/Cdots and NG/Cdots/Fe_3O_4 hybrid electrodes, two electrode configurations made from both symmetric ((NG/Fe_3O_4)//(NG/Fe_3O_4), (NG/Cdots)//(NG/Cdots) and (NG/Cdots/Fe_3O_4)//(NG/Cdots/Fe_3O_4)) and asymmetric ((NG/Cdots)//(NG/Fe_3O_4), (NG/Cdots)//(NG/Cdots/Fe_3O_4) and (NG/Fe_3O_4)//(NG/Cdots/Fe_3O_4) devices were fabricated and electrochemical measurements were performed. Figure 5A shows the CV curves of different electrode devices at sweeping rates from 5 to 100 mV/s. All the CV profiles showed relatively quasi-rectangular shapes, with close to ideal EDLC behavior and without observable redox peaks because of the rich NG contents in all the electrodes. The specific voltametric capacitances from the CV results were computed and plotted in Figure 5B. The specific capacitances decreased with the increasing scan rate. The results of the measurement of the specific capacitance indicate that higher capacitance was achieved in asymmetric the devices than in the symmetric devices and, in addition, that the symmetric (NG/Cdots/Fe_3O_4)//(NG/Cdots/Fe_3O_4) and asymmetric (NG/Fe_3O_4)//(NG/Cdots/Fe_3O_4) devices were the best symmetric and asymmetric devices, respectively. Furthermore, when the CV profiles of these devices were recorded over the potential window from 0.8 to 1.6 V at a sweep rate of 5 mV/s, the CV profiles took on similar shapes, as shown in Figure 5C, indicating that an electrode is stable at different potential windows, the specific capacitance increases with the potential window and the specific capacitance of asymmetric devices is superior to that of symmetric devices (see Figure 5D).

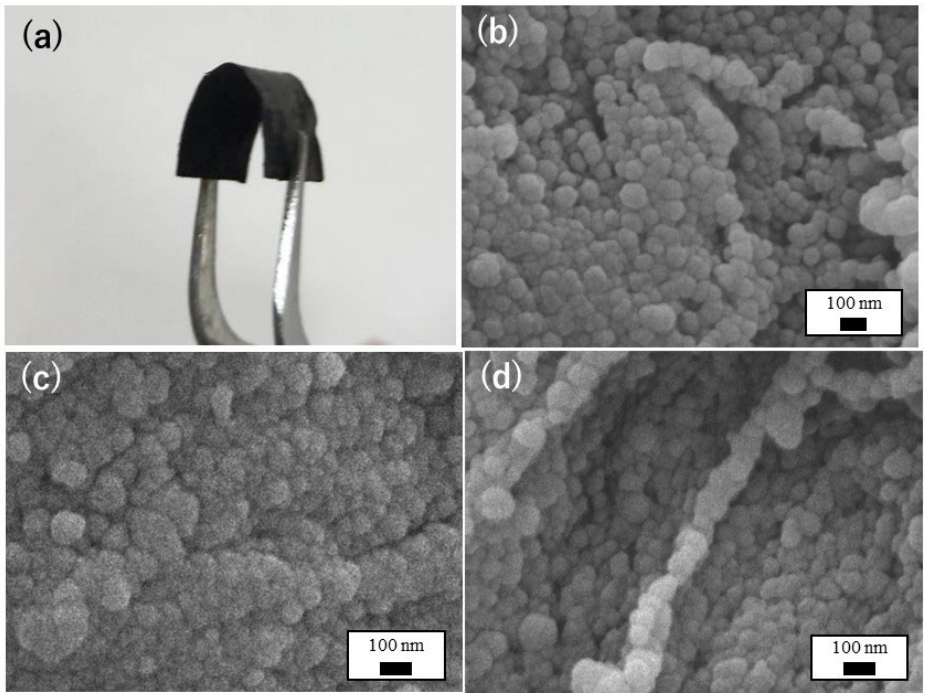

Figure 4. (**a**) An image of a bent Cdots/PPy/Fe_3O_4/TOCNF composite film. The FESEM images of Cdots/PPy/Fe_3O_4/TOCNF composite film (**b**) in a pristine state, (**c**) after bending 50 times and (**d**) after electrochemical measurement.

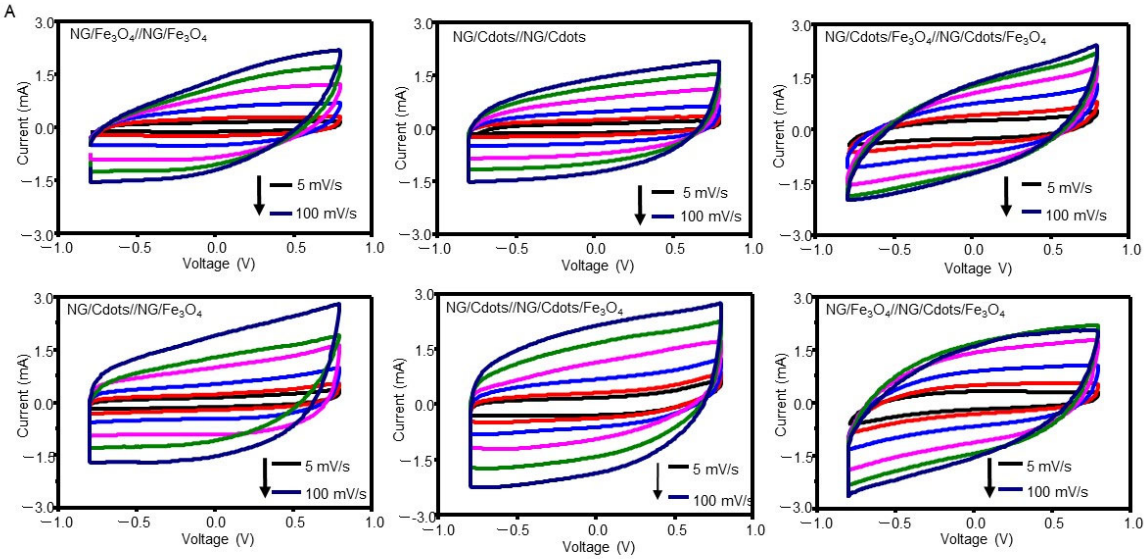

Figure 5. *Cont.*

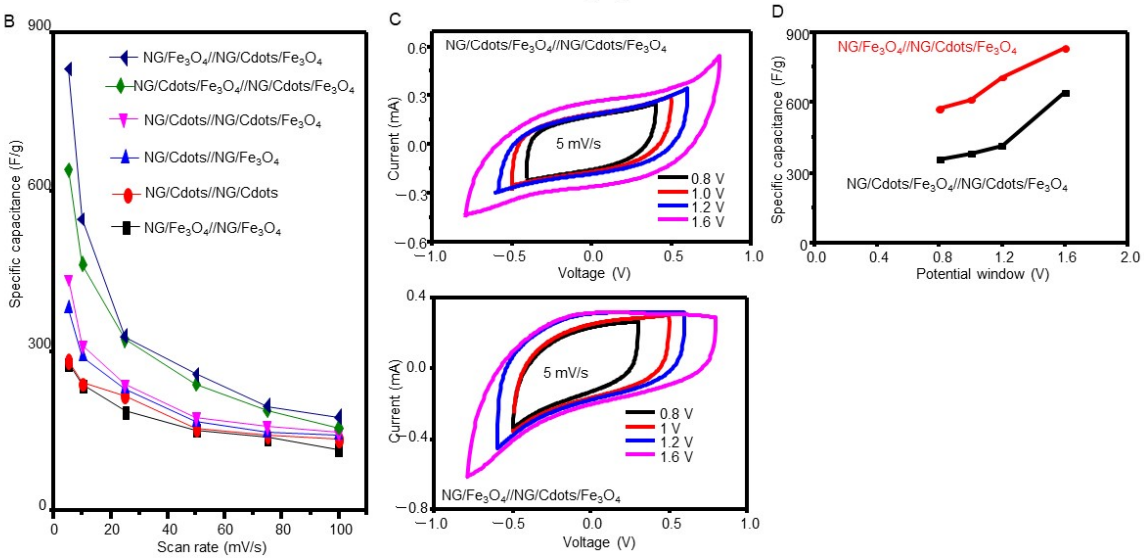

Figure 5. (**A**) CV profiles at different scan rates, (**B**) the specific capacitance as a function of scan rate, (**C**) CV profiles for different potential windows scanned at 5 mV/s and (**D**) the specific capacitance as a function of potential window at 5 mV/s for symmetric and asymmetric supercapacitors.

The GCD profiles collected at different current densities (from 0.5 to 5 A/g) are displayed in Figure 6A. The GCD revealed a near-symmetric triangle and no severe voltage drop was recorded in any of the symmetric- and asymmetric-electrode devices, indicating the low internal resistance, fast ion diffusion and excellent reversibility of charge/discharge processes [3]. As shown in Figure 6B, the gravimetric specific capacitance decreased with the increasing current density. Moreover, the asymmetric devices always showed greater specific capacitance at 0.5 A/g than the symmetric devices, while the capacitances of the symmetric ($NG/Cdots/Fe_3O_4$)//($NG/Cdots/Fe_3O_4$) and asymmetric (NG/Fe_3O_4)//($NG/Cdots/Fe_3O_4$) devices were the highest among the symmetric and asymmetric devices, respectively. The extended study on the GCD profile at 0.5 A/g over various potentials (0.8 to 1.6 V) of these two devices is shown in Figure 6C, where it is shown that all the curves measured over the potential window maintained their symmetric shapes. The discharging time increased with the potential window; hence, the gravimetric specific capacitance increased. The obtained gravimetric capacitance increased from 104 and 108 F/g at 0.8 V to 212.0 and 252.2 F/g at 1.6 V for the symmetric and asymmetric supercapacitors, respectively (see Figure 6D), indicating that the potential window can affect the gravimetric capacitance. The behaviors of the GCD were consistent with those of the CV.

The gravimetric energy density and power density, which are important parameters in the evaluation of energy-storage devices, were calculated from the gravimetric specific capacitances at different current densities and presented as a Ragone plot in Figure 6E. The energy density increased in the same manner as the increase in the gravimetric capacitance and the power density decreased with the increasing energy density. Thus, the maximum energy density obtained from the asymmetric (NG/Fe_3O_4)//($NG/Cdots/Fe_3O_4$) was 90.1 Wh/kg at a power density of 400 W/kg. This numerical value of the energy density was comparable to or better than those of the reported asymmetric devices in Table 1 [20–22,30–34].

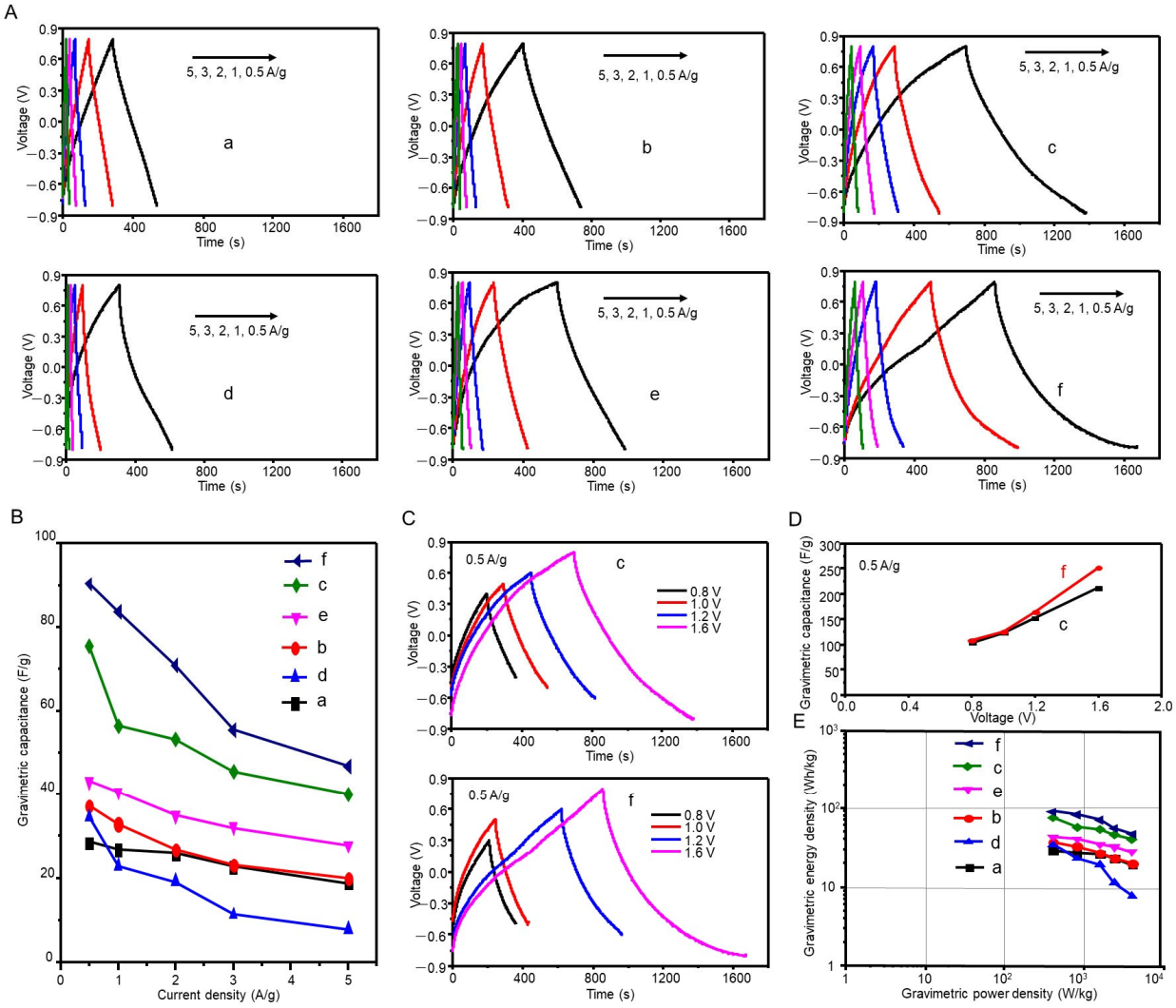

Figure 6. (**A**) The GCD profiles at different current densities and (**B**) gravimetric capacitances as a function of current density of (a–c) symmetric and (d–f) asymmetric supercapacitors. (**C**) The GCD profiles for different potential windows and (**D**) gravimetric capacitances as a function of potential window of (c) symmetric and (f) asymmetric supercapacitors at 0.5 A/g current density. (**E**) Ragone plots of (a–c) symmetric and (d–f) asymmetric supercapacitors. Supercapacitors: (a) (NG/Fe_3O_4)//(NG/Fe_3O_4), (b) (NG/Cdots)/NG/Cdots), (c) NG/Cdots/Fe_3O_4)//(NG/Cdots/Fe_3O_4), (d) (NG/Cdots)//(NG/Fe_3O_4), (e) (NG/Cdots)//(NG/Cdots/Fe_3O_4) and (f) (NG/Fe_3O_4)//(NG/Cdots/Fe_3O_4).

Table 1. Comparison of gravimetric capacitance, energy density, power density and capacitance retention for asymmetric supercapacitor devices measured with different electrolytes over wide voltage ranges.

Asymmetric Device *	Electrolyte	Potential Window (V)	Gravimetric Capacitance (F/g)	Energy Density (Wh/kg)	Power Density (W/kg)	Capacitance Retention (%) (Cycle Number)	R_s (Ω)	R_{ct} (Ω)	Ref.
AC/$Co(OH)_2$/Ni foam	6 M KOH	1.6	59.2	20.3	90.6	69 (1000)	-	2.20	33
AC/$Ni(OH)_2$/XC-72	6 M KOH	1.6	92.2	36	490.7	85 (1000)	0.18	0.10	30
Ni_3S_2/MWCNT-NC//AC	2 M KOH	1.6	55.8	19.8	798	90 (5000)	-	0.70	34
AC//$Ni(OH)_2$/EG	6 M KOH	1.6	64.6	32.3	504.7	79 (1000)	0.16	-	21
MnO_2/rGO//AC	1 M H_2SO_4	2.0	255	119.3	500	84.5 (10,000)	-	-	32
GF-CNT@Fe_2O_3//GF-$CoMoO_4$	2 M KOH	1.6	210	74.7	1400	95.4 (50,000)	-	-	31
VS_2//AC	6 M KOH	1.4	155	42	700	99 (5000)	2.97	-	20
V_2O_5@3DGr//Fe_3O_4@3DGr	1 M Na_2SO_4	1.8	122	54.9	898	89.6 (10,000)	-	-	22
(NG/Fe_3O_4)/(NG/Cdots/Fe_3O_4)	1 M NaCl	1.6	252.2	90.1	400.0	90.8 (5000)	28.0	5.8	present

* AC, commercial activated carbon; XC-72, Vulcan XC-72; MWCNT-NC, conductive multiwalled carbon nanotubes; EG, expanded graphite; rGO, reduced graphene oxide; GF-CNT, hierarchical graphite foam-carbon nanotube; GF-$CoMoO_4$, $CoMoO_4$ nanohoneycomb on graphite foam; 3DGr, three-dimensional porous graphene-wrapped.

To characterize the electrode performance in the energy-storage and -conversion devices, the EIS was measured by applying a time-varying electric potential with a small perturbing amplitude (such as 10 mV) at a few different frequencies. The resistances and differential capacitance can be identified from the Nyquist plot [35]. As shown in the fitting circuit shown in the inset of Figure 7A, the solution resistance (R_s), the double layer capacitance (C_{dl}), the Warburg impedance (W_d), the charge transfer resistance (R_{ct}) and the limiting capacitance (C_L) obtained were 15.1 Ω, 8.6 μF, 106.1 $\Omega/s^{1/2}$, 9.3 Ω and 84.6 mF, respectively, for the symmetric (NG/Cdots/Fe_3O_4)//(NG/Cdots/Fe_3O_4) and 28.0 Ω, 4.6 μF, 47.9 $\Omega/s^{1/2}$, 5.8 Ω and 6.2 mF, respectively, for the asymmetric (NG/Fe_3O_4)//(NG/Cdots/Fe_3O_4) device. The lower charge-transfer resistance from the asymmetric device than that from the symmetric device indicates that the ion diffusion of electroactive species was faster (with better ionic conductivity), the charge-transfer process was faster and the limiting capacitance was lower for the asymmetric device than for the symmetric device. This difference may have originated from the induction of an electric charge at the electrode–electrolyte interface in the material structure. Thus, the former device offers higher capacitance performance and, hence, a greater ability to store high energy density. The Bode phase plot (Figure 7B) was used to analyze the relaxation-time constant. The minimum time (relaxation time, 0.25 μs) required to discharge the energy stored from the electrode with an efficiency greater than 50% [36] was faster for the asymmetric device than for the symmetric device (0.74 μs). This result suggests that the fast charge-transfer process at the electrode–electrolyte interface in the relevant hybrid electrodes resulted in an improvement in the supercapacitor's basic ability to provide high gravimetric-energy density at higher power, as demonstrated in Figure 6E. Thus, in addition to the contribution of the intrinsic EDLS (graphene) and PC (Fe_3O_4) capacitance materials, the performance in specific capacitance was due to the contribution of the nitrogen-containing groups in the NG and Cdots with electron-transfer ability in the composites, which can shorten the electron-transfer-path length and increase electrical conductivity. Additionally, the mesoporous nature of the high specific surface area and the large pore size of NG can also contribute to the charge transfer at the interface of electrodes and electrolytes.

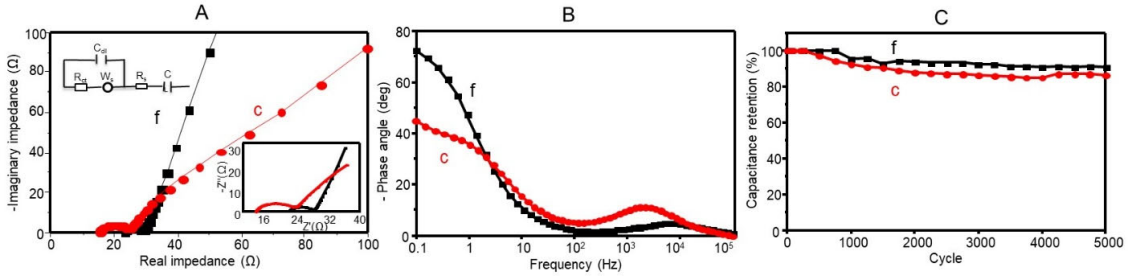

Figure 7. (**A**) Nyquist plots, (**B**) Bode phase plots and (**C**) capacitance retention of (c) symmetric (NG/Cdots/Fe_3O_4)//(NG/Cdots/Fe_3O_4)) and (f) asymmetric ((NG/Fe_3O_4)//(NG/Cdots/Fe_3O_4)) devices.

The capacitance cycling stability test is the basic gauge with which to evaluate the cycling life of devices for practical use. The stability tests over 5000 continuous cycles for the symmetric (NG/Cdots/Fe_3O_4)//(NG/Cdots/Fe_3O_4) and asymmetric (NG/Fe_3O_4)//(NG/Cdots/Fe_3O_4) devices were performed using GCD over a potential range of −0.8 to 0.8 V at a current density of 10 A/g. Figure 7C shows the obtained results of the capacitance retention versus the cycling number. Both devices demonstrated retentions of 86.5 and 90.8%, respectively. The retention recorded from the asymmetric (NG/Fe_3O_4)//(NG/Cdots/Fe_3O_4) device was comparable with the values reported for other asymmetric devices, listed in Table 1. The retention loss of 9% may have been due to the corrosion formed on the current collector (ITO). The high energy-density ability and preferable cycling performance of the asymmetric (NG/Fe_3O_4)/(NG/Cdots/Fe_3O_4) device may have been related to the meso-

porous nature of the hybrid, its high specific surface area and the large size of its pores [5,23]. Magnetite with small particle sizes attached to NG and NG/Cdots can increase the active sites for the storage of high levels of energy. Carbon dots with a fast electron-transfer ability in the hybrid can shorten electron-path length and increase electrical conductivity.

In addition, the two-electrode systems were also evaluated for the Cdots/PPy/Fe_3O_4/TOCNF film-based cells. In this study, the two-electrode systems were prepared through two combinations: two Cdots/PPy/Fe_3O_4/TOCNF films assembled as a symmetric cell and a Cdots/PPy/Fe_3O_4/TOCNF film combined with a Cdots/PPy/TOCNF film as an asymmetric cell. They are referred to as the symmetric (Cdots/PPy/Fe_3O_4/TOCNF)//(Cdots/PPy/Fe_3O_4/TOCNF) cell and the asymmetric (Cdots/PPy/Fe_3O_4/TOCNF)//(Cdots/PPy/TOCNF) cell. The specific capacitance evaluated from the CV curves increased with the decreasing scan rate, as shown in Figure 8A. The specific capacitance of 323.4 F/g for the symmetric cell at a scan rate of 5 mV/s was better than that (190.3 F/g) of the asymmetric cell. The GCD curves of both the symmetric and the asymmetric cells presented an obvious ohmic (IR) drop, and this phenomenon reduced the charging and discharging efficiency, as seen in Figure 8B. The specific capacitance (456.4 F/g) of the symmetric cell was better than that (107.1 F/g) of the asymmetric cell.

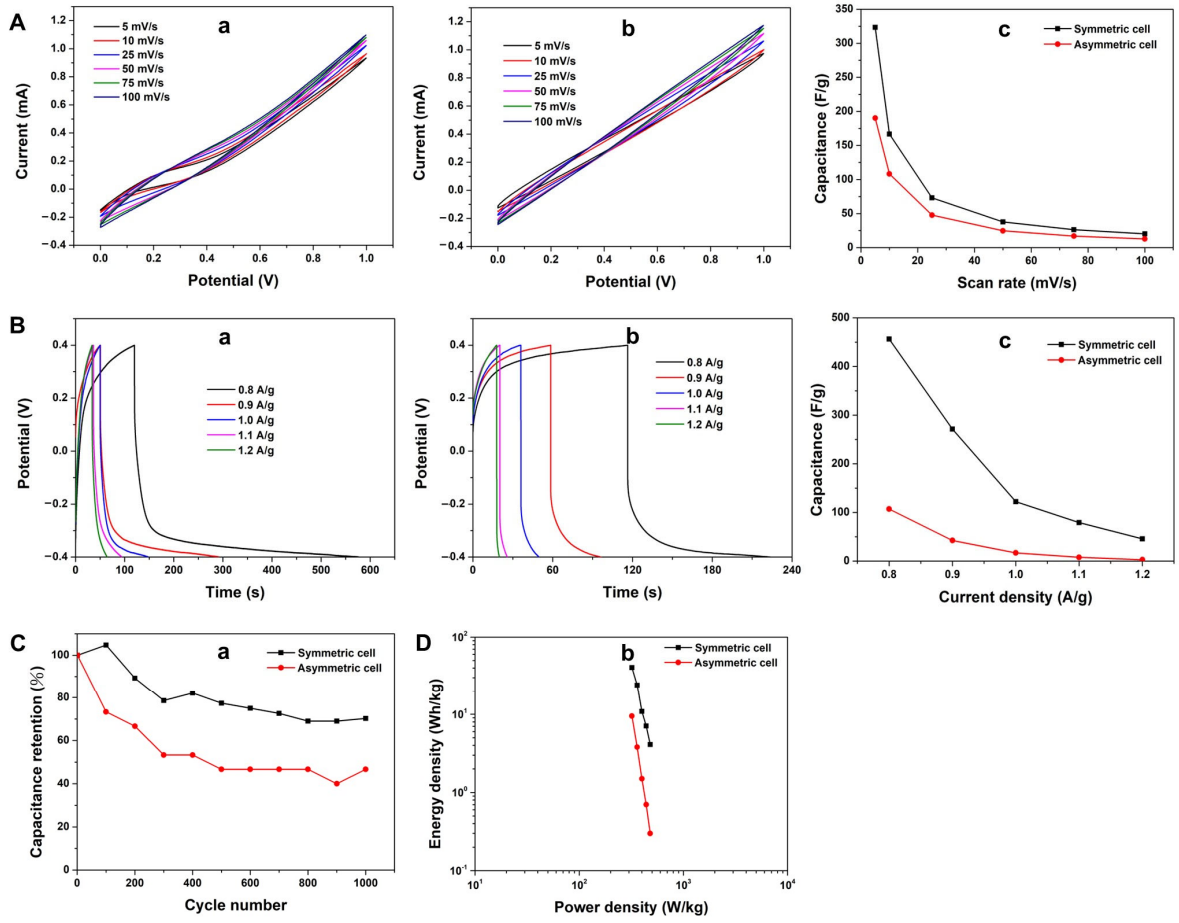

Figure 8. (**A**) CV and (**B**) GCD curves of (**a**) symmetric (Cdots/PPy/Fe_3O_4/TOCNF)//(Cdots/PPy/Fe_3O_4/TOCNF) cell and (**b**) asymmetric (Cdots/PPy/Fe_3O_4/TOCNF)//(Cdots/PPy/TOCNF) cell and (**c**) specific capacitance at various scan rates. (**C**) Cycle stabilities and (**D**) a Ragone diagram of symmetric and asymmetric cells.

The cycle stability of the symmetric and asymmetric cells for 1000 cycles was evaluated at a current density of 1.7 A/g (see Figure 8C). In the case of the symmetric cell, the specific capacitance dropped to about 80% after 200 cycles, but the tendency of the drop weakened

in the subsequent cycles. Finally, the capacitance of the cell remained at 70% for 1000 cycles. In the asymmetric cell, the specific capacitance decreased by about 20% at 100 cycles, and the cycle stability after 1000 cycles was only 47%, which was worse than that of the symmetric cell.

The gravimetric energy density and power density were assessed, as they are important indicators of electrochemical storage devices. They are displayed as Ragone diagrams (Figure 8D). The specific energy density increased with the increasing specific capacitance, but the specific power density decreased following the increase in the specific energy density. Thus, the highest energy density of 40.6 Wh/kg, of the symmetric cell, which was higher than that of the asymmetric cell, was obtained at specific power density of 320 W/kg.

No material peeled off from the surface of the composite film after the electrochemical measurement and the surface remained smooth upon visual inspection. As evidenced by the comparison between Figure 4b,d, even after the electrochemical measurement, the particle size was almost the same as before the electrochemical measurement. These results indicate that the composite film was stable and that the electrochemical testing might not have damaged it.

4. Conclusions

The electrochemical performances of symmetric and asymmetric supercapacitor devices consisting in a two-electrode configuration were compared for two series of different composition series. One series of cells was constructed from NG, Cdots, magnetite and ITO glass; typically, these featured symmetric (NG/Cdots/Fe_3O_4)//(NG/Cdots/Fe_3O_4) and asymmetric (NG/Fe_3O_4)//(NG/Cdots/Fe_3O_4) ITO cells. The capacitance performance, gravimetric energy density and capacitance retention of the asymmetric cell were higher than those of the symmetric cell. The main reason for this was the fast electron transfer between the electrode surface and the electrolyte. Another series applied was a symmetric (Cdots/PPy/Fe_3O_4/TOCNF)//(Cdots/PPy/Fe_3O_4/TOCNF)-film cell and an asymmetric (Cdots/PPy/Fe_3O_4/TOCNF)//(Cdots/PPy/TOCNF)-film cell. In this series, the capacitance performance, gravimetric energy density and capacitance retention of the symmetric cell were superior to those of the asymmetric cell and lower than in the series of NG/Cdots/Fe_3O_4. The strong IR-drop phenomenon in the Cdots/PPy/Fe_3O_4/TOCNF-series cells should be attributed to the lower supercapacitor effects in these cells than in the NG/Cdots/Fe_3O_4-series cells. These results suggest that two-electrode devices are formed not only by the components of electrodes, but also by the combination of cathode and anode electrodes. Thus, further trials are required for the development of advanced two-electrode supercapacitor devices for use as industrially applicable energy-storage devices.

Author Contributions: M.C.F., planning, experiments and writing of manuscript. P.-J.W., experiments. T.I., supervision, funding, editing and completion of manuscript. All authors have read and agreed to the published version of the manuscript.

Funding: The authors acknowledge the financial support from the Ministry of Science and Technology, Taiwan (MOST 110-2221-E-011-024-).

Institutional Review Board Statement: Not applicable.

Informed Consent Statement: Not applicable.

Data Availability Statement: All data are available through the manuscript.

Acknowledgments: M.C.F. gratefully acknowledges the National Taiwan University of Science and Technology, Taiwan, for the financial funding through the student scholarship. We also give thanks to C, M. Wu, National Taiwan University of Science and Technology, for his kind permission to use the tensile test meter.

Conflicts of Interest: The authors declare no competing financial interest.

References

1. Raghavendra, K.V.G.; Vinoth, R.; Zeb, K.; Gopi, C.V.M.; Sambasivam, S.; Kummara, M.R.; Obaidat, I.M.; Kim, H.J. An intuitive review of supercapacitors with recent progress and novel device applications. *J. Energy Storage* **2020**, *31*, 101652. [CrossRef]
2. Pandolfo, A.G.; Hollenkamp, A.F. Carbon properties and their role in supercapacitors. *J. Power Sources* **2006**, *157*, 11–27. [CrossRef]
3. Sheng, S.; Liu, W.; Zhu, K.; Cheng, K.; Ye, K.; Wang, G.; Cao, D.; Yan, J. Fe_3O_4 nanospheres in situ decorated graphene as high-performance anode for asymmetric supercapacitor with impressive energy density. *J. Colloid Interface Sci.* **2019**, *536*, 235–244. [CrossRef] [PubMed]
4. Wang, Y.G.; Li, H.Q.; Xia, Y.Y. Ordered whiskerlike polyaniline grown on the surface of mesoporous carbon and its electrochemical capacitance performance. *Adv. Mater.* **2006**, *18*, 2619–2623. [CrossRef]
5. Fite, M.C.; Rao, J.-Y.; Imae, T. Effect of External Magnetic Field on Hybrid Supercapacitors of Nitrogen-doped Graphene with Magnetic Metal Oxides. *Bull. Chem. Soc. Jpn.* **2020**, *93*, 1139–1149. [CrossRef]
6. Chang, C.C.; Geleta, T.A.; Imae, T. Effect of Carbon Dots on Supercapacitor Performance of Carbon Nanohorn/Conducting Polymer Composites. *Bull. Chem. Soc. Jpn.* **2021**, *94*, 454–462. [CrossRef]
7. Efa, M.T.; Imae, T. Hybridization of carbon-dots with ZnO nanoparticles of different sizes. *J. Taiwan Inst. Chem. Eng.* **2018**, *92*, 112–117. [CrossRef]
8. Tuerhong, M.; Yang, X.; Xue-Bo, Y. Review on carbon dots and their applications. *Chin. J. Anal. Chem.* **2017**, *45*, 139–150. [CrossRef]
9. Etefa, H.F.; Imae, T.; Yanagida, M. Enhanced Photosensitization by Carbon Dots Co-adsorbing with Dye on p-Type Semiconductor (Nickel Oxide) Solar Cells. *ACS Appl. Mater. Interfaces* **2020**, *12*, 18596–18608. [CrossRef]
10. Liu, W.; Li, C.; Ren, Y.; Sun, X.; Pan, W.; Li, Y.; Wang, J.; Wang, W. Carbon dots: Surface engineering and applications. *J. Mater. Chem. B* **2016**, *4*, 5772–5788. [CrossRef]
11. Ahmed, M.M.; Imae, T. Effect of external magnetic field on cyclic voltammetry of exfoliated graphene-based magnetic composites with conductive polymer and carbon dots. *J. Magn. Magn. Mater.* **2019**, *491*, 165604. [CrossRef]
12. Yazar, S.; Atun, G. Electrochemical synthesis of tunable polypyrrole-based composites on carbon fabric for wide potential window aqueous supercapacitor. *Int. J. Energy Res.* **2022**, *46*, 14408–14423. [CrossRef]
13. Madhuvilakku, R.; Alagar, S.; Mariappan, R.; Piraman, S. Green one-pot synthesis of flowers-like Fe_3O_4/rGO hybrid nanocomposites for effective electrochemical detection of riboflavin and low-cost supercapacitor applications. *Sens. Actuators B* **2017**, *253*, 879–892. [CrossRef]
14. Zhao, C.; Shao, X.; Zhang, Y.; Qian, X. Fe_2O_3/reduced graphene oxide/Fe_3O_4 composite in situ grown on Fe foil for high-performance supercapacitors. *ACS Appl. Mater. Interfaces* **2016**, *8*, 30133–30142. [CrossRef]
15. Ganganboina, A.B.; Chowdhury, A.D.; Doong, R.A. Nano assembly of N-doped graphene quantum dots anchored Fe_3O_4/halloysite nanotubes for high performance supercapacitor. *Electrochim. Acta* **2017**, *245*, 912–923. [CrossRef]
16. Zhang, X.; Wang, J.; Liu, J.; Wu, J.; Chen, H.; Bi, H. Design and preparation of a ternary composite of graphene oxide/carbon dots/polypyrrole for supercapacitor application: Importance and unique role of carbon dots. *Carbon* **2017**, *115*, 134–146. [CrossRef]
17. Chang, C.C.; Imae, T. Synergistic Performance of Composite Supercapacitors between Carbon Nanohorn and Conducting Polymer. *ACS Sustain. Chem. Eng.* **2018**, *6*, 5162–5172. [CrossRef]
18. Lin, T.-W.; Dai, C.-S.; Hung, K.-C. High energy density asymmetric supercapacitor based on NiOOH/Ni_3S_2/3D graphene and Fe_3O_4/graphene composite electrodes. *Sci. Rep.* **2014**, *4*, 7274. [CrossRef]
19. Wu, M.; Tong, S.; Jiang, L.; Hou, B.; Li, X.; Zhang, Y.; Yue, J.; Jiang, M.; Sheng, L. Nitrogen-doped porous carbon composite with three-dimensional conducting network for high rate supercapacitors. *J. Alloys Compd.* **2020**, *844*, 156217. [CrossRef]
20. Masikhwa, T.M.; Barzegar, F.; Dangbegnon, J.K.; Bello, A.; Madito, M.J.; Momodu, D.; Manyala, N. Asymmetric supercapacitor based on VS_2 nanosheets and activated carbon materials. *RSC Adv.* **2016**, *6*, 38990–39000. [CrossRef]
21. Yuan, J.; Tang, S.; Zhu, Z.; Qin, X.; Qu, R.; Deng, Y.; Wu, L.; Li, J.; Haarberg, G.M. Facile synthesis of high-performance $Ni(OH)_2$/expanded graphite electrodes for asymmetric supercapacitors. *J. Mater. Sci. Mater. Electron.* **2017**, *28*, 18022–18030. [CrossRef]
22. Ghaly, H.A.; El-Deen, A.G.; Souaya, E.R.; Allam, N.K. Asymmetric supercapacitors based on 3D graphene-wrapped V_2O_5 nanospheres and Fe_3O_4@3D graphene electrodes with high power and energy densities. *Electrochim. Acta* **2019**, *310*, 58–69. [CrossRef]
23. Fite, M.C.; Imae, T. Capacitance Enhancement of Nitrogen-doped Graphene Oxide/Magnetite with Polyaniline or Carbon dots Under External Magnetic Field: Supported by Theoretical Estimation. *J. Colloid Interface Sci.* **2021**, *594*, 228–244. [CrossRef] [PubMed]
24. Isogai, A. Development of completely dispersed cellulose nanofibers. *Proc. Jpn. Acad. Ser. B Phys. Biol. Sci.* **2018**, *94*, 161–179. [CrossRef] [PubMed]
25. Isogai, A.; Saito, T.; Fukuzumi, H. TEMPO-oxidized cellulose nanofibers. *Nanoscale* **2011**, *3*, 71–85. [CrossRef]
26. He, K.; Xu, C.Y.; Zhen, L.; Shao, W.Z. Hydrothermal synthesis and characterization of single-crystalline Fe_3O_4 nanowires with high aspect ratio and uniformity. *Mater. Lett.* **2007**, *61*, 3159–3162. [CrossRef]
27. Devadas, B.; Imae, T. Effect of Carbon Dots on Conducting Polymers for Energy Storage Applications. *ACS Sustain. Chem. Eng.* **2018**, *6*, 127–134. [CrossRef]
28. Krathumkhet, N.; Kao, C.-Y.; Imae, T.; Rodriguez-Abreu, C. Electrocatalytic Pt-embedded ZIF-8 on nanocellulose-based flexible conductive electrodes for hydrogen evolution reaction. *Cellulose* **2023**, 30. [CrossRef]

29. Ahangaran, F.; Hassanzadeh, A.; Nouri, S. Surface modification of Fe_3O_4@SiO_2 microsphere by silane coupling agent. *Int. Nano Lett.* **2013**, *3*, 23. [CrossRef]
30. Sui, L.; Tang, S.; Dai, Z.; Zhu, Z.; Huangfu, H.; Qin, X.; Deng, Y.; Haarberg, G.M. Supercapacitive behavior of an asymmetric supercapacitor based on a $Ni(OH)_2$/XC-72 composite. *New J. Chem.* **2015**, *39*, 9363–9371. [CrossRef]
31. Guan, C.; Liu, J.; Wang, Y.; Mao, L.; Fan, Z.; Shen, Z.; Zhang, H.; Wang, J. Iron Oxide-Decorated Carbon for Supercapacitor Anodes with Ultrahigh Energy Density and Outstanding Cycling Stability. *ACS Nano* **2015**, *9*, 5198–5207. [CrossRef]
32. Zhang, Q.; Wu, X.; Zhang, Q.; Yang, F.; Dong, H.; Sui, J.; Dong, L. One-step hydrothermal synthesis of MnO_2/graphene composite for electrochemical energy storage. *J. Electroanal. Chem.* **2019**, *837*, 108–115. [CrossRef]
33. Yang, S.; Cheng, K.; Ye, K.; Li, Y.; Qu, J.; Yin, J.; Wang, G.; Cao, D. A novel asymmetric supercapacitor with buds-like $Co(OH)_2$ used as cathode materials and activated carbon as anode materials. *J. Electroanal. Chem.* **2015**, *741*, 93–99. [CrossRef]
34. Dai, C.-S.; Chien, P.-Y.; Lin, J.-Y.; Chou, S.-W.; Wu, W.-K.; Li, P.-H.; Wu, K.-Y.; Lin, T.-W. Hierarchically structured Ni_3S_2/carbon nanotube composites as high performance cathode materials for asymmetric supercapacitors. *ACS Appl. Mater. Interfaces* **2013**, *5*, 12168–12174. [CrossRef]
35. Mei, B.-A.; Munteshari, O.; Lau, J.; Dunn, B.; Pilon, L. Physical interpretations of Nyquist plots for EDLC electrodes and devices. *J. Phys. Chem. C* **2018**, *122*, 194–206. [CrossRef]
36. Yan, J.; Wei, T.; Fan, Z.; Qian, W.; Zhang, M.; Shen, X.; Wei, F. Preparation of graphene nanosheet/carbon nanotube/polyaniline composite as electrode material for supercapacitors. *J. Power Sources* **2010**, *195*, 3041–3045. [CrossRef]